CHINESE OPTICS LETTERS

Vol. 21, No. 11 | November 2023

High-Q resonances in terahertz all-silicon metasurface with imperforated air-hole array

Qing Wang (王 青), Pengfei Wang (王鹏飞), Jianjun Liu (刘建军), Fangzhou Shu (束方洲)*, Guiming Pan (潘贵明), Zhongwei Jin (金中薇), Xufeng Jing (井绪峰), and Zhi Hong (洪 治)**

Centre for THz Research, China Jiliang University, Hangzhou 310018, China

*Corresponding author: fzshu@cjlu.edu.cn

**Corresponding author: hongzhi@cjlu.edu.cn

Received February 24, 2023 | Accepted June 26, 2023 | Posted Online November 1, 2023

We propose and experimentally demonstrate a high quality (Q)-factor all-silicon bound state in the continuum (BIC) metasurface with an imperforated air-hole array. The metasurface supports two polarization-insensitive BICs originated from guided mode resonances (GMRs) in the frequency range of 0.4 to 0.6 THz, and the measured Q-factors of the two GMRs are as high as 334 and 152, respectively. In addition, the influence of the thickness of the silicon substrate on the two resonances is analyzed in detail. The proposed all-silicon THz metasurface has great potential in the design and application of high-Q metasurfaces.

Keywords: bound state in the continuum; all-silicon metasurface; high-quality factor; terahertz.

DOI: 10.3788/COL202321.113601

1. Introduction

High quality (Q)-factor resonance is pursued in photonics to increase light–matter interactions, which is important for fundamental and applied research. In recent years, bound state in the continuum (BIC) has attracted extensive attention due to the infinite Q-factor in theory. It is a physical phenomenon in which the energy is perfectly bound to the unlimited size of the structure without any radiation[1–4]. However, due to the finite size of the structure, the absorption of the material, and other external perturbations, BIC tends to collapse to a Fano resonance with a limited radiative Q-factor. Such a resonance is known as quasi-BIC[5,6]. A metasurface provides an excellent platform to explore the BICs. Thus far, the kinds of BIC have been proposed based on multiple mechanisms, including symmetry-protected BIC[7–10], Friedrich–Wintgen BIC[11–14], resonance-trapped BIC[7,15], guided mode resonances (GMRs), and surface lattice resonance-related BIC in dimer or multimer configurations[16–22]. Owing to the ultra-high Q-factor, BIC metasurfaces have been applied in high-sensitivity sensing[23,24], ultra-low threshold lasers[7], and nonlinear harmonic generations[8,25]. Moreover, the working wavelength of BIC metasurfaces can cover from the visible to the microwave region by adjusting the structural parameters.

The terahertz (THz) band is an important region in the electromagnetic spectrum and has widespread applications in communication, sensing, and imaging. Recently, BIC metasurfaces have also been studied in the THz band. By breaking the symmetry of the structure or employing the mode coupling, BICs are achieved in metallic metasurfaces[14,26–30]. However, due to the Ohmic loss of the metal, the measured Q-factors are limited. The highest Q-factor in THz metallic BIC metasurfaces reported up to now is 227[26]. In contrast, dielectric structures lack the Ohmic loss, and electromagnetic fields are well confined in the interior of dielectric structures[31], which has great potential for achieving high-Q BIC metasurfaces[8,32–35]. However, the measured highest Q-factor in THz all-dielectric metasurfaces before 2022 is only 250 and this was achieved by designing silicon cuboids on quartz substrates[15]. In fact, a resonance with an arbitrary high-Q value can be easily designed in BIC metasurfaces theoretically by breaking the symmetry of the structure or by selecting structural parameters that deviate from those for ideal BICs. It remains a challenge to achieve this experimentally, especially at the THz band, because of the material's absorption loss, fabrication difficulty, and high spectral resolution measurements. In previous investigations of all-dielectric THz metasurfaces, most of them are realized by designing dielectric building blocks on the substrate, and interface bonding of the two bulk materials is required in device fabrication, which will not only increase the fabrication complexity but also bring about bonding defects. Thus, an all-dielectric THz metasurface made of a single material has great advantages. One direct method for generating a high-Q metasurface made of a single material is to design a complementary metasurface consisting of an air-hole array without a substrate or with a substrate made of same material. However, high-Q resonances were not

observed experimentally, and the underlying physics was not interpreted[36,37]. Recently, all-silicon BIC metasurfaces consisting of a perforated air-hole array without a substrate were reported[38,39], and the quasi-BIC resonance originated from the GMR with a record high-Q value of 1049 was experimentally achieved[38]. However, the quality of the perforated surface is difficult to control in the deep etching process.

Here, we propose and experimentally investigate an all-silicon THz BIC metasurface consisting of an imperforated air-hole array with a Si substrate, which is easier to fabricate than that without the substrate. We demonstrate that there are two quasi-BIC resonances originating from the GMR in the frequency range of 0.4 to 0.6 THz. Furthermore, the influence of thickness of the silicon substrate on the two GMRs is analyzed and compared with the metasurface without the substrate in detail. Finally, all-silicon metasurfaces with different air-hole parameters were fabricated by combining photolithography and deep reactive-ion etching, and the measured results show that Q-factors of the two GMRs are as high as 334 and 152, respectively.

2. Design and Simulation Results of All-Silicon Metasurface

2.1. Structure of an all-silicon metasurface

The schematic diagram of an all-silicon metasurface with an imperforated air-hole tetramer array is shown in Fig. 1(a). The unit cell of the metasurface contains four circular air-holes, as presented in Fig. 1(b). The structural parameters are as follows: periods of the unit cell in x- and y-directions are $P_x = P_y = 300$ μm, radii of the air-holes at the two diagonals are represented by r_1 and r_2, respectively, and the distance between the centers of the two circles along the x- and y-directions s is fixed as $s = P/2 = 150$ μm. The thickness of the metasurface is $t = t_1 + t_2 = 200$ μm, where t_1 is the depth of the air-holes, and t_2 is the thickness of the silicon substrate. The all-silicon metasurface was fabricated by combining photolithography and deep reactive-ion etching, and a scanning electron microscope (SEM) image of one fabricated metasurface is shown in Fig. 1(c). Actually, when $t_2 = 0$, the designed metasurface becomes a metasurface with a perforated air-hole array as in Ref. [38].

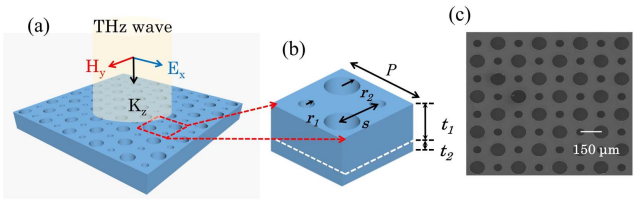

Fig. 1. (a) Schematic diagram of an all-silicon terahertz metasurface consisting of periodic imperforated air-hole tetramers when normally illuminated by a terahertz wave polarized along the x-direction. (b) Unit cell of the metasurface. The periods of the unit cell are $P_x = P_y = P = 300$ μm. The depth of air-holes is denoted as t_1, and the thickness of the substrate is t_2. (c) SEM picture of one fabricated metasurface when $r_1 = 25$ μm, $r_2 = 55$ μm, and $t_1 = 150$ μm.

2.2. Simulation results of all-silicon metasurfaces

First, we studied the optical properties of the all-silicon metasurfaces with imperforated air-hole arrays using the finite element method (COMSOL Multiphysics software). In simulation, periodic boundary conditions are employed in the x- and y-directions, whereas a perfectly matched layer (PML) is used in the z-direction. The metasurface is illuminated by the terahertz wave polarized along x-axis at normal incidence, and the dielectric constant of the silicon is set to be 11.67. Figure 2(a) shows the calculated transmission spectra of the metasurface with different r_1, where r_2 and t_1 are fixed at 55 μm and 150 μm, respectively. When $r_1 = 25$ μm, we can find that there are two strong Fano resonances located at 0.489 THz and 0.521 THz, respectively, which are labeled as f_1 and f_2. Actually, the resonances are polarization-insensitive according to the geometric symmetry of the structure. The frequency and Q-factor of the Fano resonance are obtained by fitting the transmittance curve T with the following Fano formula[40–42]:

$$T(\omega) = T_0 + A_0 \frac{[q + 2(\omega - \omega_0)/\gamma]^2}{1 + [2(\omega - \omega_0)/\gamma]^2}, \tag{1}$$

where q is the Fano fitting parameter that determines the asymmetry of resonance curve; ω_0 and γ represent resonance angular

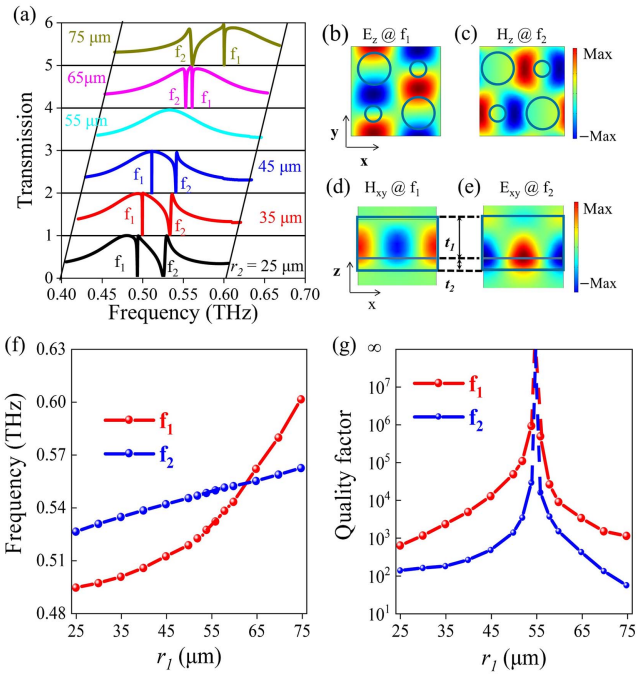

Fig. 2. (a) Simulated transmittances of the metasurface with different r_1, when $r_2 = 55$ μm. (b)–(e) Near-field electric and magnetic field distributions of resonances f_1 and f_2 at 0.489 THz and 0.521 THz, when $r_1 = 25$ μm. (f) Resonance frequencies of f_1 and f_2 with respect to r_1. (g) Q-factors of f_1 and f_2 versus r_1.

frequency and bandwidth, respectively; T_0 is transmittance baseline; and A_0 is the coupling coefficient, and therefore $Q = \omega_0/\gamma$.

To understand the properties of the two resonances, we calculated the near-field electric field and magnetic field distributions (E_z and H_z) at frequencies of the resonances f_1 and f_2. As shown in Figs. 2(b)–2(e), $H_z \approx 0$ for resonance f_1, while $E_z \approx 0$ for f_2. Therefore, resonance f_1 is a transverse magnetic (TM) mode, while f_2 is a transverse electric (TE) mode. In addition, the electromagnetic fields of f_1 are well confined within the air-hole layer, while more electromagnetic fields of f_2 are distributed within the substrate. It can also be seen from Fig. 2(a) that both the resonances f_1 and f_2 blue shift with the increase of r_1. The variation of the resonance frequencies of f_1 and f_2, as a function of r_1, is illustrated in Fig. 2(f). When r_1 increases from 25 μm to 75 μm, the blue shift of the resonance f_1 is about 107 GHz, while the blue shift is only 36 GHz for the resonance f_2. This can be explained as the electromagnetic field of resonance f_1 being mainly distributed inside the air-hole structure layer. Hence, it is very sensitive to r_1, while the electromagnetic field of f_2 is distributed in both the structure layer and the substrate. Thus, it is less sensitive to r_1. It can also be seen that the two curves cross, but the coupling of the two modes does not occur. We also retrieve the Q-factor of resonances f_1 and f_2 with a different r_1 according to the calculated transmission spectra, as shown in Fig. 2(g). We can find that when r_1 increases from 25 μm to 55 μm, both Q-factors of the resonances f_1 and f_2 increase quickly, whereas they decrease rapidly with the increase of r_1 when r_1 is larger than 55 μm. In particular, when $r_1 = r_2 = 55$ μm, the two resonances f_1 and f_2 disappear in the transmission spectrum, and the Q-factors of resonances f_1 and f_2 approach infinite, which is a typical characteristic of BICs.

In order to further understand this phenomenon, we calculated the dispersion curves of the metasurface when $r_1 = r_2 = 55$ μm. As shown in Fig. 3(a), there are four eigenmodes related to the resonances f_1 and f_2. Two TM modes near 0.53 THz are denoted as TM 1 and TM 2, while two TE modes near 0.55 THz are denoted as TE 1 and TE 2. Q-factors of the four eigenmodes are all close to infinity at $\Gamma = 0$ and off Γ as well.

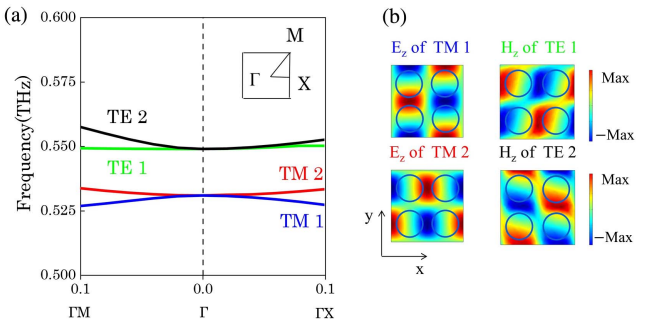

Fig. 3. (a) Dispersion curves of the four related TE and TM eigenmodes, as a function of k $P/2\pi$, when $r_1 = r_2 = 55$ μm, where k is a propagating constant. The inset shows the first Brillouin zone of the square lattice. (b) Electric (E_z) and magnetic (H_z) near-fields in the xy plane of the four modes at $\Gamma = 0$.

We also calculated the electromagnetic field distributions of the four modes at $\Gamma = 0$, as shown in Fig. 3(b). TM 1 and TM 2 are two TM guide modes propagating along 45° and −45° relative to the x-axis, respectively, which are induced by (1, 1) Rayleigh diffraction of 2D metagrating with a period of P[17,38,43]. Similar to the two TM modes, TE 1 and TE 2 are two TE guide modes induced by (1, 1) diffraction of 2D metagrating. Therefore, when $r_1 = r_2 = 55$ μm, both resonances f_1 and f_2 are ideal BICs that originated from the GMR[17,44]. When the lattice symmetry is broken ($r_1 \neq r_2$), the two BIC modes are transformed into two quasi-BIC modes with a finite Q-factor, which can be observed experimentally. From above calculations, we can get that the two resonances f_1 and f_2 of the metasurface consisting of the air-hole array with or without the substrate are essentially the same, except for different frequencies and Q values.

2.3. Effect of substrate on resonance characteristics

In previous calculations, the depth of the air-holes t_1 is fixed at 150 μm and the thickness of the substrate t_2 is fixed at 50 μm. In the following, we discuss the effect of the substrate on the two GMRs. We calculated the transmission spectra of the metasurface, where the depth of the air-holes t_1 is changed from 130 μm to 200 μm, and t is fixed at 200 μm. The variation of the resonance frequencies of f_1 and f_2, as a function of r_1, is illustrated in Figs. 4(a) and 4(c), respectively. As t_1 increases from 130 μm to 200 μm, i.e., the thickness of the substrate t_2 decreases from 70 μm to 0 μm, both resonances f_1 and f_2 have blue shifts, as is usually the case[13]. Since f_2 is more sensitive to the thickness of the substrate than f_1, the blue shift of f_2 is larger than that of f_1. For example, when $r_1 = 30$ μm, the resonance f_1 has only a

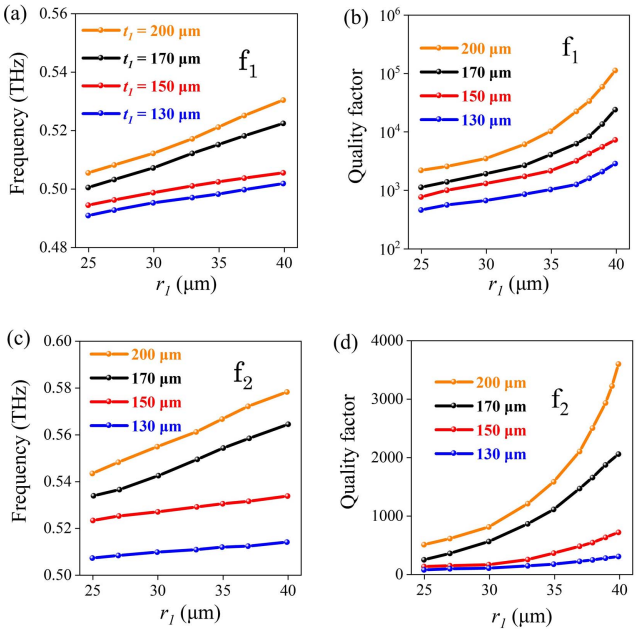

Fig. 4. (a), (c) Influence of air-hole depth t_1 on the frequency and (b), (d) Q-factor of the resonances f_1 and f_2, when thickness of metasurface $t = 200$ μm.

blue shift of about 17 GHz, while the blue shift for f_2 is 45 GHz. In addition, the frequency of the resonance f_2 gradually becomes sensitive to r_1, as the thickness of the substrate decreases. Figures 4(b) and 4(d) show the influence of the depth of air-holes t_1 on the Q-factors of the two resonances. The Q-factors of resonances f_1 and f_2 increase quickly with the increase of t_1, that is, the electromagnetic field confinements of the two resonances are enhanced, leading to a decrease in the radiation loss of the two modes. Further, when t_1 is less than 150 μm, the Q-factor of f_2 is very low, but it rises rapidly when t_1 increases from 150 μm to 200 μm, because much more electromagnetic field distribution of f_2 switches from the substrate to the air-hole layer. The results show that the addition of the substrate greatly reduces the Q values of the two GMRs.

3. Experimental Results

To demonstrate previous simulated results, we fabricated and measured the transmission spectra of the all-silicon metasurfaces with an imperforated air-hole array. In experiments, the designed metasurfaces were fabricated in a high-resistivity silicon wafer ($> 5000\ \Omega \cdot$ cm) with a thickness of 200 μm because of its low loss and mature fabrication technique. According to the structure shown in Fig. 1(a), four all-silicon metasurfaces with a size of 15 mm × 15 mm were fabricated through photolithography and followed by deep reactive ion etching (Bosch process), where $t_1 = 150$ μm, $r_2 = 55$ μm, and r_1 was chosen as 25 μm, 30 μm, 35 μm, and 40 μm, respectively. An SEM picture of one of the fabricated samples ($r_1 = 25$ μm) is shown in Fig. 1(c). We used a high spectral resolution (140 MHz) terahertz frequency-domain spectroscopy system (TeraScan 1550 from Toptica) to measure the transmission spectra of the four samples. In measurements, the terahertz wave radiated from the photoconductive antenna by photomixing is collimated and focused by 2.54 cm off-axis parabolic lenses with 75 mm focal length and normally incident on the metasurfaces. The measurements were done at room temperature and in dry air conditions (humidity ≤1%) to eliminate the effects of water vapor absorption, and the integration constant was set to be 300 ms to enhance the signal-to-noise ratio (SNR) of the measurement.

Considering both the error of the air-hole radius in the fabrication and the loss caused by defects, we recalculated the transmission spectra of the metasurface by adding 2 μm to the designed air-hole radius and a loss tangent of 0.0003 to the equivalent material loss of the silicon, as shown in Fig. 5(a). The measured transmission spectra are also shown in Fig. 5(b). Figures 5(c) and 5(d) are enlarged views of the measured resonances f_2 and f_1 and their Fano fitting curves, respectively. It can be seen that a strong resonance f_2 is observed in all four samples, meanwhile resonance f_1 is clearly measured in three samples, but it is not observed in the sample $r_1 = 40$ μm because of its high-Q factor (1370 calculated). It is well known that the higher the Q-factor of the resonance, the more susceptible it is to the material's absorption, fabrication defects, or device size. The

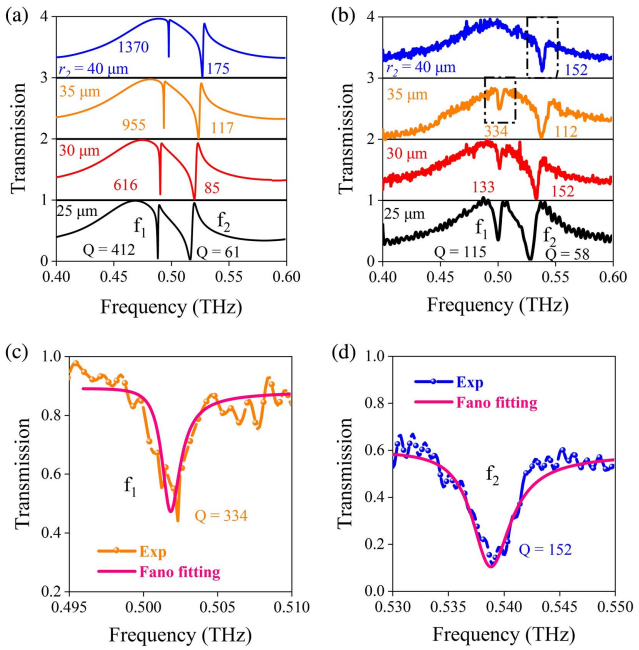

Fig. 5. (a) Calculated and (b) measured transmittances of four metasurfaces. (c) and (d) Enlarged views of measured resonance f_2 for the sample r_1 = 40 μm (blue) and f_1 for the sample r_1 = 35 μm (yellow) and their Fano fitted curves (pink).

measured frequencies of the two resonances are in good agreement with the recalculated results. In addition, the Q-factors of the two resonances f_1 and f_2 increase with the increase of r_1 as expected. For resonance f_2, the measured Q-factors are very close to those recalculated with equivalent material loss. This is because the Q-factor of f_2 is low (≤ 175 calculated and ≤ 152 measured), and it will not be largely influenced by the material loss and fabrication defects, while the Q-factors of resonance f_1 are much larger than those of resonance f_2. For example, for the three metasurfaces $r_1 = 25$ μm, 30 μm, and 35 μm, the calculated Q-factors are 412, 616, and 955, respectively, but the measured values are only 115, 133, and 334, smaller than the calculated ones. Compared with the previous all-dielectric THz BIC metasurfaces, which design dielectric building blocks on the substrate, the measured Q-factor is improved based on the all-silicon THz BIC metasurface containing an air-hole array as done in this work. However, it is smaller than that we reported in the corresponding all-silicon metasurface with a perforated air-hole array without using a substrate[38].

4. Conclusion

In summary, we propose and experimentally demonstrate an all-silicon BIC metasurface consisting of an air-hole tetramer array with a Si substrate. The metasurface supports two polarization-insensitive BIC resonances originated from the GMR in the frequency range of 0.4–0.6 THz, and their Q-factors can be adjusted flexibly by changing the air-hole radius. The characteristics of the two GMRs with different thickness of the substrate

are numerically investigated. The results show that Q-factors of the two resonances without the substrate are much larger than those with the substrate. In addition, they can be improved by increasing the depth of the air-holes. Finally, the designed all-silicon metasurfaces are fabricated by combining photolithography and deep reactive-ion etching, and the measured Q-factors of the two GMRs are as high as 334 and 152, respectively. As high-Q silicon devices are very sensitive to changes in refractive index or absorption of silicon materials, the proposed metasurface can be used as efficient THz switches or modulators by exploring its photon induced carrier absorption effect, and the optical pump power can be remarkably reduced.

Acknowledgement

This work was supported by the National Natural Science Foundation of China (Nos. 61875179, 12004362, and 62175224).

References

1. D. C. Marinica, A. G. Borisov, and S. V. Shabanov, "Bound States in the continuum in photonics," Phys. Rev. Lett. **100**, 183902 (2008).
2. C. W. Hsu, B. Zhen, J. Lee, S.-L. Chua, S. G. Johnson, J. D. Joannopoulos, and M. Soljačić, "Observation of trapped light within the radiation continuum," Nature **499**, 188 (2013).
3. Y. K. Srivastava, R. T. Ako, M. Gupta, M. Bhaskaran, S. Sriram, and R. Singh, "Terahertz sensing of 7 nm dielectric film with bound states in the continuum metasurfaces," Appl. Phys. Lett. **115**, 151105 (2019).
4. S. I. Azzam and A. V. Kildishev, "Photonic bound states in the continuum: from basics to applications," Adv. Opt. Mater. **9**, 2001469 (2021).
5. Z. F. Sadrieva, I. S. Sinev, K. L. Koshelev, A. Samusev, I. V. Iorsh, O. Takayama, R. Malureanu, A. A. Bogdanov, and A. V. Lavrinenko, "Transition from optical bound states in the continuum to leaky resonances: role of substrate and roughness," ACS Photonics **4**, 723 (2017).
6. H. M. Doeleman, F. Monticone, W. den Hollander, A. Alù, and A. F. Koenderink, "Experimental observation of a polarization vortex at an optical bound state in the continuum," Nat. Photonics **12**, 397 (2018).
7. A. Kodigala, T. Lepetit, Q. Gu, B. Bahari, Y. Fainman, and B. Kante, "Lasing action from photonic bound states in continuum," Nature **541**, 196 (2017).
8. Z. Liu, Y. Xu, Y. Lin, J. Xiang, T. Feng, Q. Cao, J. Li, S. Lan, and J. Liu, "High-Q quasibound states in the continuum for nonlinear metasurfaces," Phys. Rev. Lett. **123**, 253901 (2019).
9. K. Koshelev, S. Lepeshov, M. Liu, A. Bogdanov, and Y. Kivshar, "Asymmetric metasurfaces with high-Q resonances governed by bound states in the continuum," Phys. Rev. Lett. **121**, 193903 (2018).
10. K. Fan, I. V. Shadrivov, and W. J. Padilla, "Dynamic bound states in the continuum," Optica **6**, 169 (2019).
11. H. Friedrich and D. Wintgen, "Interfering resonances and bound states in the continuum," Phys. Rev. A **32**, 3231 (1985).
12. M. V. Rybin, K. L. Koshelev, Z. F. Sadrieva, K. B. Samusev, A. A. Bogdanov, M. F. Limonov, and Y. S. Kivshar, "High-Q supercavity modes in subwavelength dielectric resonators," Phys. Rev. Lett. **119**, 243901 (2017).
13. F. He, J. Liu, G. Pan, F. Shu, X. Jing, and Z. Hong, "Analogue of electromagnetically induced transparency in an all-dielectric double-layer metasurface based on bound states in the continuum," Nanomaterials **11**, 2343 (2021).
14. X. Zhao, C. Chen, K. Kaj, I. Hammock, Y. Huang, R. D. Averitt, and X. Zhang, "Terahertz investigation of bound states in the continuum of metallic metasurfaces," Optica **7**, 1548 (2020).
15. S. Han, L. Cong, Y. K. Srivastava, B. Qiang, M. V. Rybin, A. Kumar, R. Jain, W. X. Lim, V. G. Achanta, S. S. Prabhu, Q. J. Wang, Y. S. Kivshar, and R. Singh, "All-dielectric active terahertz photonics driven by bound states in the continuum," Adv. Mater. **31**, 1901921 (2019).
16. A. C. Overvig, S. Shrestha, and N. Yu, "Dimerized high contrast gratings," Nanophotonics **7**, 1157 (2018).
17. W. Shi, J. Gu, X. Zhang, Q. Xu, J. Han, Q. Yang, L. Cong, and W. Zhang, "Terahertz bound states in the continuum with incident angle robustness induced by a dual period metagrating," Photonics Res. **10**, 810 (2022).
18. F. Wu, J. Wu, Z. Guo, H. Jiang, Y. Sun, Y. Li, J. Ren, and H. Chen, "Giant enhancement of the Goos–Hänchen shift assisted by quasibound states in the continuum," Phys. Rev. Appl. **12**, 014028 (2019).
19. Y. He, G. Guo, T. Feng, Y. Xu, and A. E. Miroshnichenko, "Toroidal dipole bound states in the continuum," Phys. Rev. B. **98**, 161112 (2018).
20. S. Murai, D. R. Abujetas, L. B. Liu, G. W. Castellanos, V. Giannini, J. A. Sánchez-Gil, K. Tanaka, and J. G. Rivas, "Engineering bound states in the continuum at telecom wavelengths with non-Bravais lattices," Laser Photonics Rev. **16**, 2100661 (2022).
21. H. Kwon, T. Zheng, and A. Faraon, "Nano-electromechanical tuning of dual-mode resonant dielectric metasurfaces for dynamic amplitude and phase modulation," Nano Lett. **21**, 2817 (2021).
22. Y. H. Ko, K. J. Lee, F. A. Simlan, and R. Magnusson, "Singular states of resonant nanophotonic lattices," Nanophotonics **12**, 263 (2023).
23. A. Tittl, A. Leitis, M. Liu, F. Yesilkoy, D.-Y. Choi, D. N. Neshev, Y. S. Kivshar, and H. Altug, "Imaging-based molecular barcoding with pixelated dielectric metasurfaces," Science **360**, 1105 (2018).
24. F. Yesilkoy, E. R. Arvelo, Y. Jahani, M. Liu, A. Tittl, V. Cevher, Y. Kivshar, and H. Altug, "Ultrasensitive hyperspectral imaging and biodetection enabled by dielectric metasurfaces," Nat. Photonics **13**, 390 (2019).
25. L. Carletti, K. Koshelev, C. De Angelis, and Y. Kivshar, "Giant nonlinear response at the nanoscale driven by bound states in the continuum," Phys. Rev. Lett. **121**, 033903 (2018).
26. W. Cao, R. Singh, I. A. I. Al-Naib, M. He, A. J. Taylor, and W. Zhang, "Low-loss ultra-high-Q dark mode plasmonic Fano metamaterials," Opt. Lett. **37**, 3366 (2012).
27. D. R. Abujetas, N. van Hoof, S. ter Huurne, J. Gómez Rivas, and J. A. Sánchez-Gil, "Spectral and temporal evidence of robust photonic bound states in the continuum on terahertz metasurfaces," Optica **6**, 996 (2019).
28. L. Cong and R. Singh, "Symmetry-protected dual bound states in the continuum in metamaterials," Adv. Opt. Mater. **7**, 1900383 (2019).
29. E. Mikheeva, K. Koshelev, D.-Y. Choi, S. Kruk, J. Lumeau, R. Abdeddaim, I. Voznyuk, S. Enoch, and Y. Kivshar, "Photosensitive chalcogenide metasurfaces supporting bound states in the continuum," Opt. Express **27**, 33847 (2019).
30. X. Li, J. Yin, J. Liu, F. Shu, T. Lang, X. Jing, and Z. Hong, "Resonant transparency of a planar anapole metamaterial at terahertz frequencies," Photonics Res. **9**, 125 (2021).
31. S. Jahani and Z. Jacob, "All-dielectric metamaterials," Nat. Nanotechnol. **11**, 23 (2016).
32. J. Li, J. Li, C. Zheng, Z. Yue, D. Yang, S. Wang, M. Li, Y. Zhang, and J. Yao, "Spectral amplitude modulation and dynamic near-field displaying of all-silicon terahertz metasurfaces supporting bound states in the continuum," Appl. Phys. Lett. **119**, 241105 (2021).
33. S. Han, P. Pitchappa, W. Wang, Y. K. Srivastava, M. V. Rybin, and R. Singh, "Extended bound states in the continuum with symmetry-broken terahertz dielectric metasurfaces," Adv. Opt. Mater. **9**, 2002001 (2021).
34. P. Hong, L. Xu, and M. Rahmani, "Dual bound states in the continuum enhanced second harmonic generation with transition metal dichalcogenides monolayer," Opto-Electron. Adv. **5**, 200097 (2022).
35. C. Fang, Q. Yang, Q. Yuan, X. Gan, J. Zhao, Y. Shao, Y. Liu, G. Han, and Y. Hao, "High-Q resonances governed by the quasi-bound states in the continuum in all-dielectric metasurfaces," Opto-Electron. Adv. **4**, 200030 (2021).
36. Z. Wang, L. Chen, X. Li, T. Lang, X. Jing, and Z. Hong, "Analogue of electromagnetically-induced transparency with ultra-narrow bandwidth in a silicon terahertz metasurface," Opt. Mater. Express **11**, 1943 (2021).
37. Y. Liu, Y. Luo, X. Jin, X. Zhou, K. Song, and X. Zhao, "High-Q Fano resonances in asymmetric and symmetric all-dielectric metasurfaces," Plasmonics **12**, 1431 (2017).
38. P. Wang, F. He, J. Liu, F. Shu, B. Fang, T. Lang, X. Jing, and Z. Hong, "Ultra-high-Q resonances in terahertz all-silicon metasurfaces based on bound states in the continuum," Photonics Res. **10**, 2743 (2022).

39. W. Wang, Y. K. Srivastava, T. C. Tan, Z. Wang, and R. Singh, "Brillouin zone folding driven bound states in the continuum," Nat. Commun. **14**, 2811 (2023).
40. M. Galli, S. L. Portalupi, M. Belotti, L. C. Andreani, L. O'Faolain, and T. F. Krauss, "Light scattering and Fano resonances in high-Q photonic crystal nanocavities," Appl. Phys. Lett. **94**, 071101 (2009).
41. I. S. Maksymov and A. E. Miroshnichenko, "Active control over nanofocusing with nanorod plasmonic antennas," Opt. Express **19**, 5888 (2011).
42. M. F. Limonov, M. V. Rybin, A. N. Poddubny, and Y. S. Kivshar, "Fano resonances in photonics," Nat. Photonics **11**, 543 (2017).
43. Z. Yu, H. Chen, J. Liu, X. Jing, X. Li, and Z. Hong, "Guided mode resonance in planar metamaterials consisting of two ring resonators with different sizes," Chin. Phys. B **26**, 077804 (2017).
44. J. Fan, Z. Li, Z. Xue, H. Xing, D. Lu, G. Xu, J. Gu, J. Han, and L. Cong, "Hybrid bound states in the continuum in terahertz metasurfaces," Opto-Electron. Sci. **2**, 230006 (2023).